The 3D ultrastructural morphology of a marine ammonia-oxidizing archaeon

Yangkai Zhou[1]*, An Yan[2]*, Jiawen Yang[2,3]*, Wei He[1]*, Shuai Guo[2,3], Yifan Li[1], Yanchao Dai[4], Xijiang Pan[4], Dongyu Cui[1], Olivier Pereira[1,5], Wenkai Teng[1], Ran Bi[1], Songze Chen[1], Lu Fan[1], Peiyi Wang[2], Yan Liao[6], Wei Qin[7], Sen-Fang Sui[2,8], Yuanqing Zhu[1,9], Chuanlun Zhang[1,9]†, Zheng Liu[2]†

[1] Shenzhen Key Laboratory of Marine Archaea Geo-Omics, Department of Ocean Science and Engineering, Southern University of Science and Technology, Shenzhen, Guangdong, China

[2] Cryo-electron Microscopy Center, Southern University of Science and Technology, Shenzhen, Guangdong, China

[3] Department of Biology, Southern University of Science and Technology, Shenzhen, Guangdong Province, China

[4] Shanghai NanoPort, Thermo Fisher Scientific Inc., Shanghai, China

[5] Institut AMU-WUT, Aix-Marseille Université and Wuhan University of Technology, Wuhan, Hubei, China

[6] Australian Institute for Microbiology & Infection, University of Technology Sydney, Ultimo, Australia

[7] School of Biological Sciences and Institute for Environmental Genomics, University of Oklahoma, Norman, Oklahoma, USA

[8] State Key Laboratory of Membrane Biology, Beijing Frontier Research Center for Biological Structures, Beijing Advanced Innovation Center for Structural Biology, School of Life Sciences, Tsinghua University, Beijing, China

[9] Shanghai Sheshan National Geophysical Observatory, Shanghai, China

* These authors contributed equally.

† Correspondence: Chuanlun Zhang (zhangcl@sustech.edu.cn), Zheng Liu (liuz3@sustech.edu.cn).

Abstract

Nitrososphaerota, formerly known as *Thaumarchaeota*, constitute a diverse and widespread group of ammonia-oxidizing archaea (AOA) inhabiting ubiquitously in marine and terrestrial environments, playing a pivotal role in global nitrogen cycling. Despite their significance in Earth's ecosystems, the cellular organization of AOA remains largely unexplored, leading to a significant question unanswered of how the machinery of these organisms underpins metabolic functions. In this study, we combined chromatic-aberration-corrected cryo-electron tomography (cryo-ET), scanning transmission electron microscopy (STEM), and energy dispersive X-ray spectroscopy (EDS) to unveil the cellular organization and elemental composition of *Nitrosopumilus maritimus* SCM1, a representative member of marine *Nitrososphaerota*. Our tomograms show the native ultrastructural morphology of SCM1 and one to several dense storage granules in the cytoplasm. STEM-EDS analysis identifies two types of storage granules in which one type is possibly composed of polyphosphate, while the other type is polyhydroxyalkanoate. Collectively, these findings provide visual evidence for the resilience of AOA in the vast oligotrophic marine environment.

Introduction

Comprehending the intricate cellular structure of microorganisms holds paramount importance in advancing our understanding of metabolic functions in ecology, evolution, and biogeochemistry (González-Pech et al., 2023). Despite remarkable advancements in cryo-electron microscopy (cryo-EM) technology and the potential value of archaeal structural biology in medical and industrial applications (Shin et al., 2014), the realm of structural biology of marine archaea remains relatively underexplored, necessitating efforts to comprehensively grasp their cellular structure and physiological mechanisms (Lipp et al., 2008; Stahl and de la Torre, 2012).

Ammonia-oxidizing archaea (AOA), belonging to the currently classified *Nitrososphaerota*, derive energy from the oxidation of ammonia to nitrite, initiating nitrification process that is vital in the aquatic nitrogen cycle (Stahl and de la Torre, 2012; Walker et al., 2010). The resulting nitrite, a byproduct of AOA activity, can be further transformed into nitrate by nitrite-oxidizing bacteria, and ultimately eliminated from the ecosystem as it converts into nitrogen gas through denitrifying bacteria (Martikainen, 2022). Notably, *Nitrosopumilus maritimus* SCM1 stands out as the first isolate of AOA (Konneke et al., 2005), exemplifying one of the most prevalent ammonia-oxidizing microbes in the oceans and actively driving global nitrogen cycling.

Previous studies have delved into various aspects of *Nitrosopumilus maritimus* SCM1, including its physiology like ammonium oxidation, stress adaptation, carbon fixation, genome, metabolome, lipidome, evolution and ecology (Abby et al., 2020; Hodgskiss et al., 2023; Kim et al., 2019; Kitzinger et al., 2020, 2019; Kraft et al., 2022; Law et al., 2021a, 2021b; Leavitt et al., 2023; Li et al., 2018; Martens-Habbena et al., 2009; Qin et al., 2020, 2018, 2014; Walker et al., 2010; Wan et al., 2023; Yang et al., 2021). However, our knowledge of its cellular structure remains limited. Within an archaeal cell, the cellular components are organized in a specific

79 arrangement. Starting from the cell surface and moving inward, these components
80 typically include an s-layer, pseudoperiplasmic space, cytoplasmic membrane,
81 nucleoid, ribosomes. Additionally, certain archaeal cells may possess additional
82 structures like vesicles, archaellum and storage granules (van Wolferen et al.,
83 2022). Several studies have reported the presence of S-layer proteins on the
84 surface of SCM1 cells, suggesting its existence as a cell wall (Qin et al., 2017;
85 Urakawa et al., 2011). Additionally, high abundance of ribosomes numbering
86 ~1000 in each cell has been observed in SCM1 (Urakawa et al., 2011), which likely
87 provide advantage in coping with extreme environmental conditions (Yin et al.,
88 2018).
89

90 However, the cellular structure of AOA, including for example the presence and
91 function of storage granules, remains inadequately understood due to limited
92 research efforts. Storage granules play a pivotal role in microorganisms by
93 enabling them to withstand fluctuations in nutrient availability. Although extensive
94 investigations have been conducted on storage granules in certain bacterial,
95 thermophilic archaea, and eukaryotic organisms (Gal et al., 2017; Sarkar et al.,
96 2021; Tocheva et al., 2013; Toso et al., 2011, 2016; Ward et al., 2012), their
97 existence and functionality in marine archaea, particularly in SCM1, have yet to be
98 explored in detail (Qin et al., 2017; Urakawa et al., 2011). This knowledge gap
99 necessitates further exploration to unravel the cellular structure and evaluate the
100 presence and function of storage granules in marine archaea, and thereby
101 expanding our understanding in this uncharted domain.
102

103 This study aimed to address the knowledge gap in structural biology of AOA by
104 employing cutting-edge techniques that combine chromatic-aberration-corrected
105 cryo-electron microscopy (cryo-EM), cryo-electron tomography (cryo-ET),
106 scanning transmission electron microscopy (STEM), and energy-dispersive X-ray
107 spectroscopy (EDS). These technologies allowed us to visualize the cell
108 morphology of the AOA type strain *Nitrosopumilus maritimus* SCM1 at ultra-high

resolution, which demonstrated the presence of two types of storage granules and cell division patterns. These findings provide new insight into the potential metabolic functions of storage granules in marine archaea, while shedding light on the high-resolution characteristics of SCM1 cells in energy storage. The use of chromatic-aberration-corrected cryo-ET, which was pioneered in this study, represents an innovative technology for effectively and comprehensively visualizing both archaeal and bacterial cells at submicron scales.

Results

Whole-cell cryo-electron tomography of *Nitrosopumilus maritimus* SCM1

We monitored cell growth in *Nitrosopumilus maritimus* SCM1 cultures by analyzing nitrite concentration. As shown in **Supplementary Figure 1**, during the nine days' cultivation period, nitrite concentration continued rise in the first seven days. We harvested SCM1 cells between day 6 and day 8, corresponding to the middle to later exponential phase. The purity of the cultures was evaluated using the qPCR method, and the results are presented in **Supplementary Table 1**.

Initially, we examined the morphology of *Nitrosopumilus maritimus* SCM1 cells by traditional cryo-EM. Our observations revealed that SCM1 cells showed a typical rod shape, with diameters ranging from 320 to 410 nm, lengths spanning from 590 to 1350 nm and the mean length-diameter ratio around 2.43 ± 0.57 (**Supplementary Figure 2**). Subsequently, cryo-ET experiment elucidated the cellular organization of SCM1 cells and provided a native three-dimensional (3D) structural information of the cell. Given the considerable thickness of the SCM1 (averaged diameter ~360nm, **Supplementary Figure 2**), the tilt-series image acquisition could not be completed. The thickness would double at ±60°, rendering it unsuitable for conventional cryo-EM data acquisition (**Supplementary Figure 3**). To overcome this difficulty, we employed the first chromatic-aberration-corrected cryo-EM in the world, of which can increase a signal/noise ratio for the thick specimens by corrected inelastic scattering. With the Cc corrector, images can be obtained at ±60°, and 3D tomogram can be reconstructed with less missing wedges. The 3D structure of native SCM1 revealed a highly organized proteinaceous surface layer (S-layer) enveloping the entire cell surface, and cell membrane exhibited well-defined, smooth, and continuous features (**Figure 1** and **Supplementary Movie 1**). Notably, an area rich in nucleic acids and dozens of ribosomes were observed in the cytoplasm of SCM1 (**Figure 1** and **Figure 2**) Interestingly, the number of ribosomes in SCM1 were ranged between 30-100 in each cell, which appeared to be significantly less than those found in eukaryotes

(Xing et al., 2023) or other prokaryotes (Xue et al., 2022) that observed by cryo-ET, lending a support for the slow growth of SCM1 that typically observed in the laboratory culture (**Supplementary Figure 1**). Moreover, this result highlights the superior accuracy of cryo-ET in quantifying ribosomes at the three-dimensional level compared to counting them in two-dimensional microscopic images (Urakawa et al., 2011).

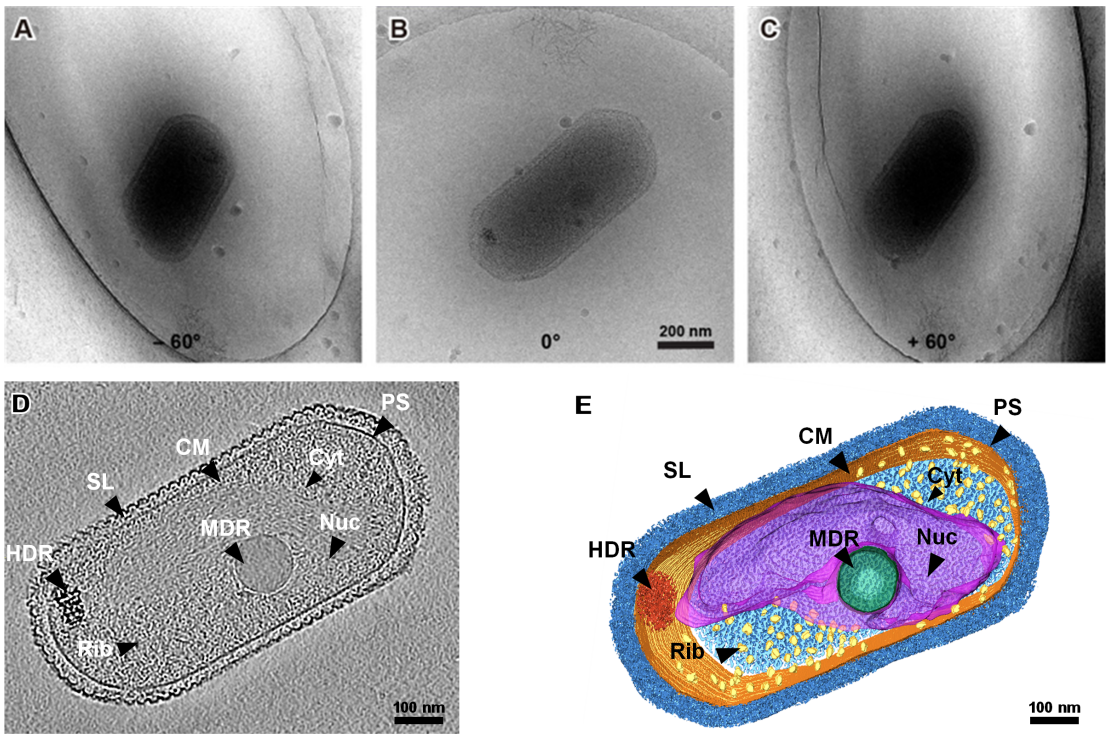

Figure 1. Whole-cell cryo-electron tomogram of *Nitrosopumilus maritimus* SCM1.

(A-C) Cryo-EM images of SCM1 at – 60°, 0°, and + 60° angles. (D) Central section through a tomogram showed the cellular structure of SCM1. (E) 3D segmentation of SCM1 cell. MDR, medium-density region; HDR, high-density region; CM, cytoplasmic membrane; SL, surface layer; Nuc, nucleoid; Rib, ribosome; PS, pseudoperiplasmic space; and Cyt, cytoplasm, are displayed.

157 **Observation of cell division in *Nitrosopumilus maritimus* SCM1**

158 We examined several cells in the exponential phase and identified instances of
159 unequal divisions (**Figure 2A** and **2B**). The central region of SCM1 first exhibited
160 constriction, followed by elongation towards two ends before eventually dividing
161 into two cells. Notably, the cell division of SCM1 did not follow a homomorphic
162 pattern, with the larger daughter cell assuming an oblate spheroidal shape,
163 resembling the shape of another independently observed cell in **Figure 2C** and **2D**.
164 Additionally, we observed a putative budding state of SCM1 (**Figure 2E** and **2F**).
165

166 Moreover, to determine the predominant mode of SCM1 cell division, we
167 conducted an intense measurement to observe changes in the diameter and length
168 of SCM1 in the late exponential phase. The results revealed two significant
169 decreases in the length of SCM1 within a 48-hour period, occurring at 11 PM on
170 the Day 6 and 7 AM on the Day 7, respectively (**Figure 2G**). However, no notable
171 change in diameter was observed within the 48-hour timeframe. The time interval
172 between the two decreasing points aligns with the doubling time of SCM1 (Td $\approx$
173 30 h, **Supplementary Figure 2**), indicating a high level of synchronicity in cell
174 division.
175

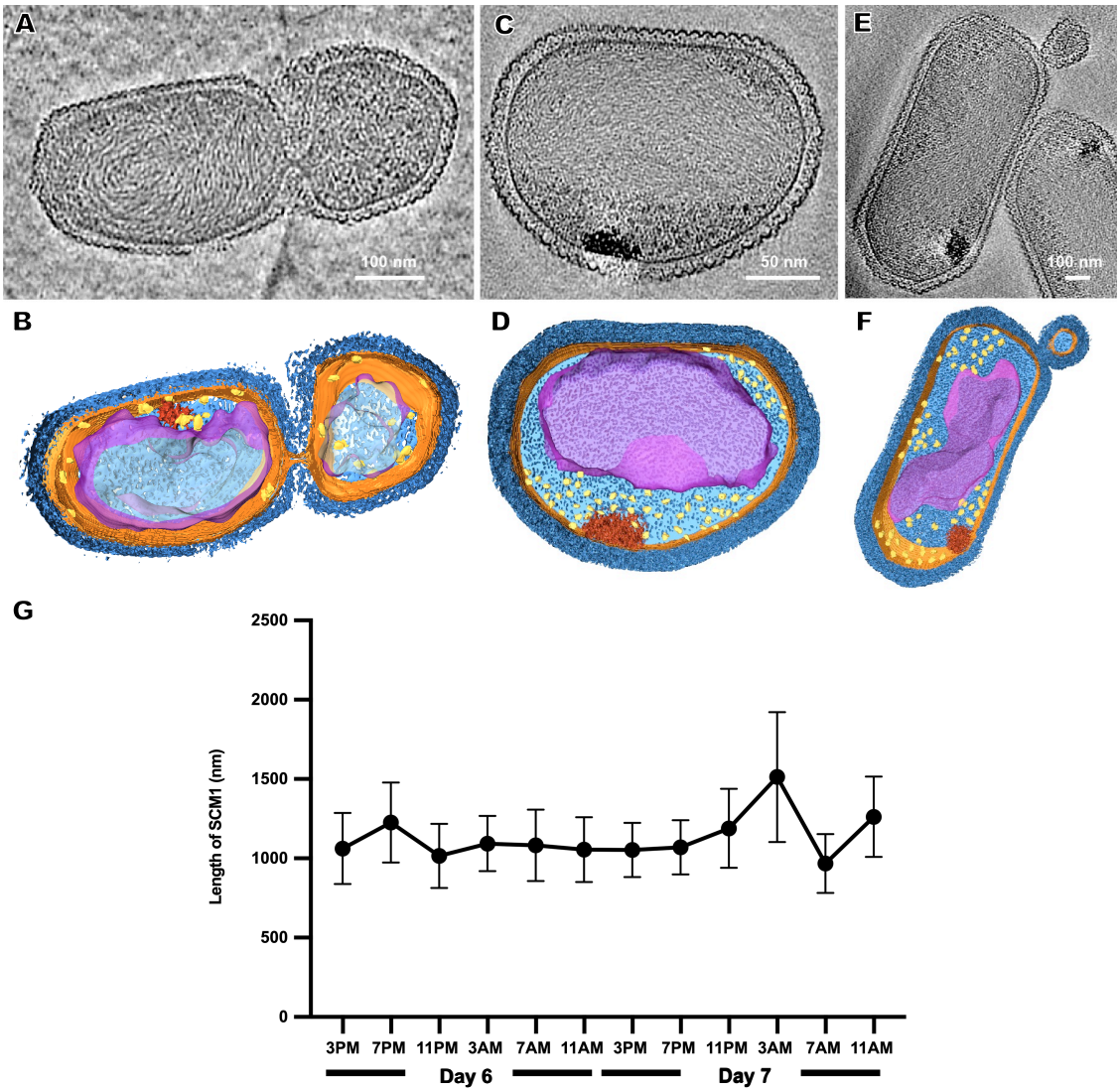

Figure 2. Observation of cell division in *Nitrosopumilus maritimus* SCM1. (A, C, E) Slices through tomograms of SCM1 in the exponential phase. (B, D, F) 3D segmentation of (A, C, E). S-layer (dark blue), cell membrane (orange); cytoplasm (light blue); nucleoid (purple); ribosomes (yellow); high-density region (red). (G) The average length of SCM1 at different time points. SCM1 cells were analyzed every 4 hours for 48 hours period in the late exponential phase (*n* = 40).

177 **Characterization of intracellular storage granules**

178 Our cryo-ET results revealed density regions corresponding to granule in the
179 cytoplasm of SCM1 (**Figure 1D** and **1E**). Based on differences in electronic density,
180 we classified them into medium-density regions (MDR) and high-density regions
181 (HDR). The MDR observed in SCM1 displayed a distinct and consistent spherical
182 morphology, with diameters typically ranging from approximately 85–185 nm, with
183 a smooth and continuous surface. The HDR exhibited an irregular shape and
184 comprised varying electronic density. Most HDRs were situated at the edge of cell,
185 near the cell membrane (**Figure 1** and **Figure 2**).

186

187 To analyze the elemental composition of MDR and HDR granules in the SCM1
188 cells, we used a Talos F200X to obtain EDS spectra. Area scans revealed
189 differential compositions of the granules, while HDRs containing elevated
190 concentrations of calcium, phosphorus, oxygen, and magnesium, the MDRs had a
191 slight increase in carbon concentration and a slightly lower concentration of oxygen
192 (**Figure 3** and **Supplementary Table 2**). Carbon and nitrogen were the most
193 abundant elements throughout the entire scanned region across the cells.

194

195 The mean Raman spectrum of SCM1 showed main biomolecules in single cells
196 (**Figure 4A**). The Raman band at 1726 cm^{-1}, which was slightly shifted from 1739
197 cm^{-1} in *Nitrososphaera gargensis* (Spang et al., 2012), could be attributed to
198 polyhydroxyalkanoate (PHA). This shift of band was caused by the stretching of
199 the C=O ester in PHA (Izumi and Temperini, 2010). The presence of this band also
200 suggested that the PHA produced by SCM1 may have a high crystallinity (Izumi
201 and Temperini, 2010), which was consistent with the results of cryo-ET (**Figure 1**).

202

203 To further assess SCM1's potential to metabolize storage granules and fully
204 understand the metabolic potential at higher taxa, we conducted an in-depth
205 exploration of key metabolic pathways in *Nitrosopumilus maritimus* SCM1 and
206 other AOA genomes, focusing on Polyphosphate (PolyP) and
207 polyhydroxyalkanoate (PHA) metabolism. After conducting a thorough genome

208 annotation, we identified several crucial PHA metabolic genes, such as *PhaE* and
209 *PhaC*, which are responsible for PHA synthesis. Additionally, we discovered *BdhA*,
210 along with various hydratases and dehydrogenases, which play a role in PHA
211 degradation in SCM1. However, despite the presence of intracellular PolyP
212 confirmed by STEM-EDS analysis, we found no homologous genes associated
213 with PolyP synthesis and degradation, suggesting additional undiscovered genes
214 involved in PolyP metabolism in SCM1.
215
216 When considering a broader spectrum of AOA, we observed the presence of PolyP
217 and PHA metabolic genes across various strains (**Figure 4B**). Notably, PolyP
218 genes were identified in AOA strains ST2, ST3, N4, Nd1, Nd2, CS, SbT1, SR1,
219 EN76, G61, and MY3. Among these strains, only ST2 and ST3 were found in
220 marine habitats, specifically wastewater treatment beside the ocean. The
221 occurrence of *Ppk2* genes in terrestrial AOA strains (CS, SbT1, SR1, G61, MY3)
222 highlighted the ecological diversity and metabolic versatility within the AOA clade.
223

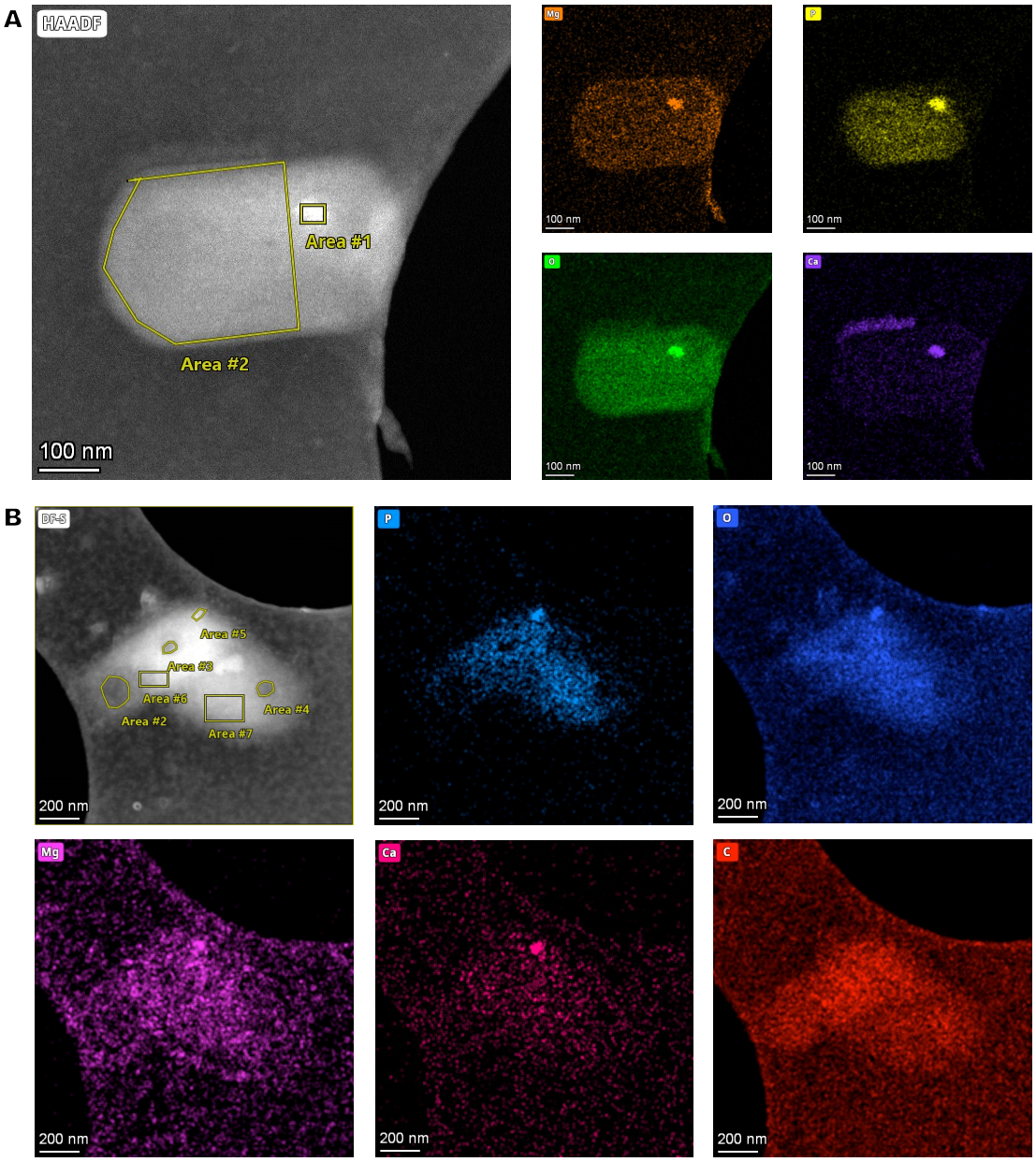

Figure 3. Elements in storage granules of SCM1.

(A) STEM images and EDS elemental analysis revealed that magnesium (Mg), phosphorus (P), oxygen (O), and calcium (Ca) in the Area #1 stood out from the background, indicating that enrichment of these elements in the HDR. (B) STEM-EDS results of two adjacent SCM1 cells. Area #5 is a HDR that enriched with Mg, P, O, and Ca. Area #2, 3, and 4 are MDRs with slightly higher concentration of carbon (C).

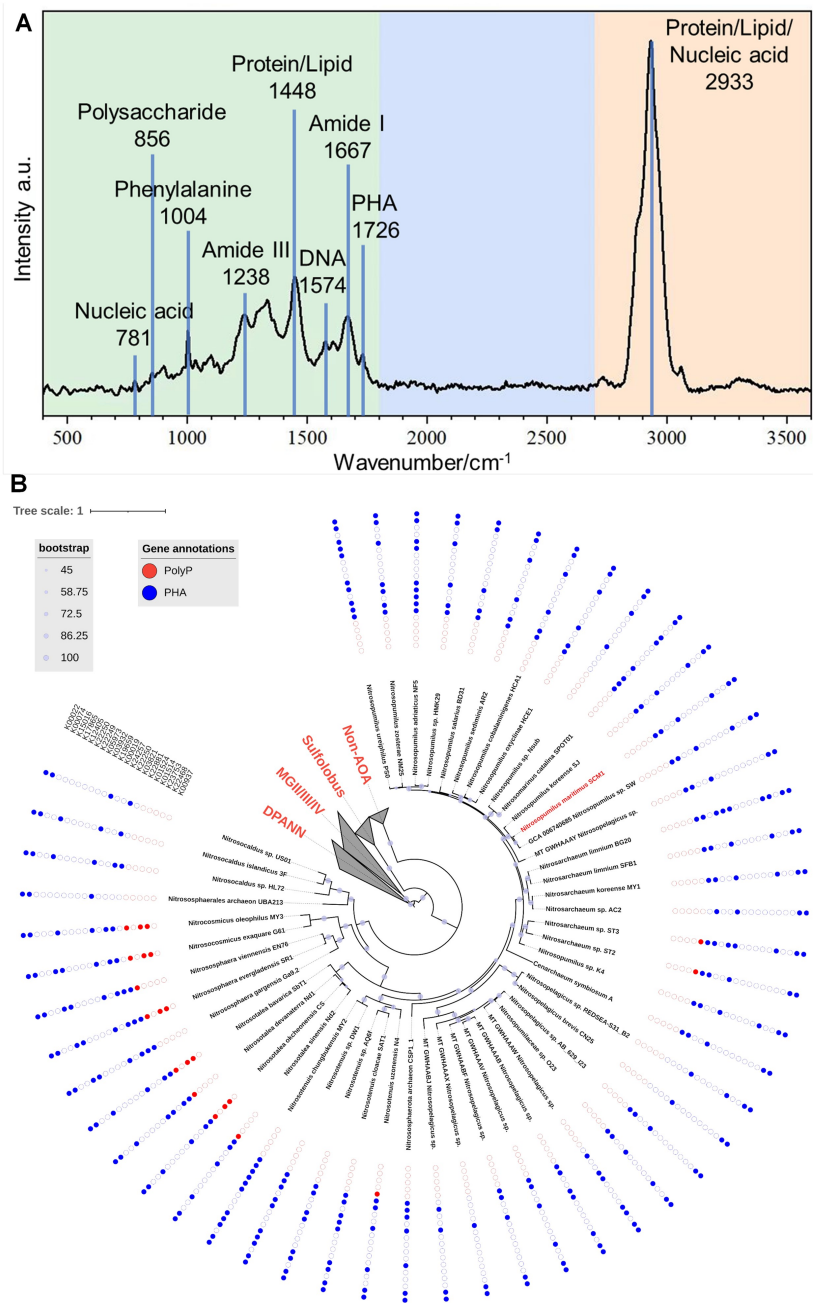

Figure 4. The Raman spectrum of *Nitrosopumilus maritimus* SCM1 and the distributions of metabolic genes regarding PolyP and PHA in AOA. (A) The mean Raman Spectrum of 33 single cells of SCM1. A characteristic peak of PHA at intensity = 1726 cm^{-1} was identified. (B) The phylogenomic tree of 51 nonredundant AOA genomes. The presence or absence of metabolic genes related to PolyP and PHA annotated by KEGG are shown around the tree. Solid dots: presence of the gene, empty dots: absence of the gene.

Discussion

According to previous studies, SCM1 owns two cell division systems in the genome, but only uses one system, the Cdv system, correlated with the eukaryotic ESCRT-III machinery, for cell division (Pelve et al., 2011; van Wolferen et al., 2022). However, the function of FtsZ system in SCM1 even in the whole *Nitrososphaerota* phylum, is not yet fully understood. Only one study has reported that the absence of polymerization function prevents FtsZ from participating in the cell division process (Ng et al., 2013). Based on the cryo-EM images we captured, we not only observed SCM1 cells in the fission state but also identified cells potentially in the budding state (**Figure 2E** and **2F**), suggesting the activation of the FtsZ system during the budding process. However, given the limited number of SCM1 cells we observed in the budding state, we cannot rule out the possibility of them being extracellular membrane vesicles, similar to those found in haloarchaea *Haloferax volcanii* (Ring and Eichler, 2001; Shalev et al., 2017; Tamir and Eichler, 2017).

Nutrition storage is crucial for microorganisms, providing resilience against fluctuations in nutrient availability. In the previous studies involving bacteria and archaea, similar storage granules had been analyzed using both electron energy loss spectroscopy (EELS) and energy dispersive X-ray spectroscopy (EDS) to determine their elemental composition (Lechaire et al., 2002; Remonsellez et al., 2006). In this study, STEM-EDS analysis has unveiled the intricate elemental composition of intracellular storage granules within *Nitrosopumilus maritimus* SCM1. The HDR granules exhibit heightened levels of phosphate, oxygen, and metals, suggesting their potential involvement in the resilience of oligotrophic marine environments. The discovery of these storage granules opens intriguing avenues for unraveling SCM1's metabolic strategies and adaptive mechanisms.

In the early 20th century, ultrastructural investigations have already revealed the presence of polyphosphates granules in archaeal cells (Rudnick et al., 1990; Scherer and Bochem, 1983). Toso et al., introduced EDS analysis and demonstrated the high abundance of phosphorus, oxygen and cationic elements

in polyphosphate bodies in *Methanospirillum hungatei* (Toso et al., 2011), *Archaeoglobus fulgidus* (Toso et al., 2016) and ANME-2b (McGlynn et al., 2018). Consistent to previous studies, the high concentration of phosphorus and oxygen, along with cationic elements, suggests the presence of polyphosphate (PolyP) in the HDR granules, which indicated that SCM1 may have a greater contribution to global phosphorus cycling than previously recognized (Qin et al., 2020). Divalent cations, such as magnesium and calcium, were known to form ionic bonds between phosphate groups, enabling tighter packing and increased granule density (Parsons et al., 2010). In previous studies, it was believed that carboxysomes, glycogen, and polyphosphate were absent in SCM1 (Urakawa et al., 2011). Instead, an amorphous region with higher electron density, possibly containing phosphorus, was observed. However, our findings from cryo-ET and STEM-EDS analysis have confirmed the presence of polyphosphate in SCM1. This significant discovery was facilitated by advancements in technology and a heightened research focus on understanding the elemental composition of archaea cells.

The presence of PHA in SCM1, as indicated by STEM-EDS, Raman spectroscopy, genome and proteome analyses, opens avenues for understanding its physiological functions. While the exact function of PHA in SCM1 remains to be elucidate (Qin et al., 2020), its potential role in carbon and energy storage, similar to its function in haloarchaea, warrants further investigation. The existence of PHA may contribute to SCM1's capacity to adapt to severe environmental conditions or insufficient nutrient availability. The 3-hydroxypropionate/4-hydroxybutyrate (3HP/4HB) cycle, discovered in AOA, represents the most energy-efficient aerobic carbon fixation pathway currently known (Johnson et al., 2023; Konneke et al., 2014). According to the definition of the PHA synthesis/degradation pathway, Konneke et al. found a key step involving the synthesis of PHA precursors in the carbon cycle pathway of SCM1 (Konneke et al., 2014).

287 Our analysis of the PHA synthesis/degradation pathway, considering the presence
288 of key genes like *PhaEC* in the genome and proteome (**Figure 4B** and
289 **Supplementary Table 3**), suggests that under conditions of limited nutrition, such
290 as depletion of bicarbonate ions, the 3HP/4HB cycle in SCM1 may not function
291 normally. Instead, SCM1 could switch to the biosynthesis pathway of PHA, utilizing
292 carbon for survival. This adds credence to the hypothesis of PHA's presence in
293 SCM1 cells. Further exploration of the role of PHA in SCM1's metabolism promises
294 valuable insights into its adaptive strategies.
295

296 **Materials and Methods**

297

298 ***Nitrosopumilus maritimus SCM1 cultivation***

299 We followed previous protocol for SCM1 cultivation, growth monitoring, and culture
300 purity assessment (Law et al., 2021b). To ensure the absence of bacterial and
301 organic contaminants during the long-term cultivation, we used a combination of
302 0.5 μg/ml Rifamycin sodium and 1 μg/ml hydrosoluble Amphotericin B. We
303 assessed cell growth by detecting nitrite production, which was determined by
304 diazo-colorimetric assay with photometric detection at 545 nm. For evaluating
305 culture purity, we employed quantitative real-time PCR (qPCR) to accurately
306 measure the culture's integrity and absence of contaminants, detailed data are
307 provided in **Supplementary Table 1**.

308

309 ***Collection and processing of Raman spectra of Nitrosopumilus maritimus***
310 ***SCM1***

311 *Nitrosopumilus maritimus* SCM1 was incubated at 30°C for 14 days. The pre-
312 treatment processes were as described previously (Wang et al., 2021). Single-cell
313 Raman spectra were acquired using a Raman imaging microscope (WITec alpha
314 300R) with 532 nm laser. All raw spectra were preprocessed with Project Five 5.2
315 (WITec) for baseline correction and vector normalization.

316

317 ***Cryo-EM sample preparation and data acquisition***

318 Quantifoil Cu R2/1 grids were glow discharged at 15 mA for 45 seconds using a
319 Pelco easiGlow discharged unit. An aliquot of 4 μL concentrated sample of SCM1
320 was applied to the front side of the grids, then the sample was vitrified by plunge
321 freezing in a liquid ethane using a Mark IV Vitrobot (Thermo Fisher Scientific) at
322 6 °C and 100% humidity. The vitrified samples were loaded into a 300-kV Titan
323 Krios microscopy G3i (Thermo Fisher Scientific) equipped with GIF quantum
324 energy filter and K2 Summit direct electron detector (Gatan Inc.). Images were

acquired using SerialEM package (Mastronarde, 2003) by the K2 camera operated under the super-resolution mode at a nominal magnification of ×26,000 (calibrated pixel size 5.417 Å). Each micrograph was fractionated into 36 frames with a total dose of 50 $e^{-}/Å^2$. The defocus range was set from −5.0 to −8.0 μm.

Cryo-ET data collection and tomogram reconstruction

For cryo-ET, the vitrified samples were loaded into a 300-kV Titan Krios microscopy G4 (Thermo Fisher Scientific) equipped with Selectris energy filter and CEOS CCOR-spherical aberration / chromatic aberration (Cs/Cc) corrector. Tilt images were acquired by Falcon 4 camera under counting mode at a nominal magnification of ×26,000 (calibrated pixel size of 3.41 Å). A dose-symmetric scheme (Hagen et al., 2017) was used to collect tilt-series from -60° to +60° at a step size of 2° using SerialEM software (Mastronarde, 2003). Each tilt image was recorded as a video stack consisting of 10 frames with a dose of 1.64 $e^{-}/Å^2$. The defocus was set range from -4 to -6 μm and the total dose was 100 $e^{-}/Å^2$. Video frames of each tilt image were motion-corrected by MotionCor2 v.1.1.0 (Zheng et al., 2017). Tilt series were merged into one stack and aligned by patch tracking in IMOD v.4.9.12 (Kremer et al., 1996). In total, 221 sets of tilt-series were collected. The selected tomograms were reconstructed the missing-wedge information and increased signal-to-noise ratio by IsoNet (Liu et al., 2022) for display and segmentation by Amira (version 2020.3.1, Thermo Fisher Scientific).

STEM-EDS analysis

Samples were cryo-transferred by the Elsa™ holder (Gatan, model 698, ultra-low profile) and imaged in a Thermofisher Talos F200X transmission electron microscopy equipped with a Ceta camera in bright field mode, operated at a 200 kV acceleration voltage. Next, the cryo-holder with the sample was inserted into a pumping station to warm up to room temperature. Then a focused electron probe with high energy was used to stimulate a specific area of the sample. The atoms being stimulated may eject electrons, resulting in the emission of X-ray photons as a form of energy release. The energy exhibited by these X-rays is indicative of the

356 particular atomic element from which they originated. Therefore, an energy-
357 dispersive spectrometer can be employed to quantify the quantity and energy of
358 the X-rays, providing a quantitative description of the elemental composition of the
359 stimulated area of the sample (Toso et al., 2011). STEM-EDS tomography was
360 acquired at room temperature. The data process and 3D visualization were
361 performed by Inspect 3D and Avizo software.
362
363 ***Gene and genomic analysis***
364 Phylogenomic analysis of *Nitrososphaerota* was conducted using IQ-TREE with
365 GTDB archaeal markers obtained from the Genome Taxonomy Database. The
366 selected markers were carefully aligned using MAFFT and then concatenated into
367 a supermatrix. The best-fitting substitution model was determined using
368 ModelFinder, and the phylogenomic tree was constructed using Maximum
369 Likelihood with ultrafast bootstrap approximation. The genomes were curated as
370 our previous study. The PolyP and PHA were investigated in AOA after predicting
371 proteins from the AOA genomes. The obtained AOA proteins were aligned against
372 the KO profiles available in the KEGG database (accessed in November 2023).
373 The results were filtered based on the HMM score (>90), and the corresponding
374 KO related to PolyP and PHA metabolic genes were searched. Additionally, to
375 confirm our annotation, the presence of each key functional domain of the targeted
376 proteins was manually checked using InterProScan
377 (https://www.ebi.ac.uk/interpro/). The KO numbers of PolyP related genes are:
378 K00937(*Ppk1*), K22468(*Ppk2*), K23753(*Ppk2*), K01514(*PPX1*),
379 K01524(*Ppx/GppA*), and PHA related genes are: K22881(*PhaE*), K03821(*PhaC*),
380 K22250(*PhaB*), K24257(*PhaR*), K00019(*BdhA*), K19659(*PhaJ*), K03932(*PhaZ1*),
381 K05973(*PhaZ*), K22249(*PhaZ*), K22250(*PhaZ*), K12405(hydratase),
382 K17865(hydratase), K15016(hydratase), K00074(dehrogenase),
383 K00022(dehrogenase). The resulting tree was beautified using the Interactive Tree
384 of Life (iTOL) web tool. The Newick-formatted tree was uploaded to iTOL, where
385 branches were colorized, additional annotations were added, and the overall
386 appearance of the tree was customized for better clarity and aesthetics.

387

388 ***Proteome analysis***

389 Filters containing late exponential phase *Nitrosopumilus maritimus* SCM1 cells
390 were extracted using a modified protocol as described before (Qin et al., 2018),
391 either trypsin or GluC was used as protease digestion. Mass spectrometry analysis
392 was carried out at Shenzhen Wininnovate BioTechnology Co., Ltd. DDA (data-
393 dependent acquisition) mass spectrum techniques were used to acquire tandem
394 MS data on a ThermoFisher Q Exactive mass spectrometer fitted with a Nano Flex
395 ion source. The raw MS/MS spectra were treated and searched against the NCBI
396 and UniProt Proteome dataset using MaxQuant 2.0.3.0. The generated data set
397 contains the results of different hydrolases and databases for comparison.

398

399 **Acknowledgements**
400 We thank Huiqin Xu, Xiaoyun Yang, and Zongqiang Li for assistance on
401 experiment design. Jing Wu, Yuanzhu Gao, Juying Tan, and Fangfang Zhang for
402 technical support. This study was supported by the Stable Support Plan Program
403 of Shenzhen Natural Science Fund (20200925173954005), National Natural
404 Science Foundation of China (32241028 and 91851210), the Shenzhen Key
405 Laboratory of Marine Archaea Geo-Omics, Southern University of Science and
406 Technology (ZDSYS201802081843490), and the Project of Educational
407 Commission of Guangdong Province of China (2020KTSCX123). The
408 bioinformatic analyses were performed on the Tai-Yi high-performance
409 supercomputer cluster at Southern University of Science and Technology.

410

411 **Author contributions**

412 ZL, CZ designed the study. YZ, AY, JY, WH performed the sample preparation,
413 data analyses, and wrote the manuscript. SG conducted the reconstruction of cryo-
414 ET data. YL prepared cell cultures, performed the sample preparation experiment.
415 YD, XP performed the STEM-EDS analyses. DC performed the Raman spectrum
416 analyses. OP, WT, RB, SC, LF assisted the lab work or data analyses. PW, SS

provided platforms. WQ, YL assisted study design, data interpretation and manuscript editing. ZL, CZ supervised the investigation and revised manuscript.

Competing interests

The authors declare no conflict of interest.

References

Abby SS, Kerou M, Schleper C. 2020. Ancestral Reconstructions Decipher Major Adaptations of Ammonia-Oxidizing Archaea upon Radiation into Moderate Terrestrial and Marine Environments. *mBio* **11**:e02371-20. doi:10.1128/mBio.02371-20

Gal A, Sviben S, Wirth R, Schreiber A, Lassalle‐Kaiser B, Faivre D, Scheffel A. 2017. Trace‐Element Incorporation into Intracellular Pools Uncovers Calcium‐Pathways in a Coccolithophore. *Advanced Science* **4**:1700088. doi:10.1002/advs.201700088

González-Pech RA, Li VY, Garcia V, Boville E, Mammone M, Kitano H, Ritchie KB, Medina M. 2023. The Evolution, Assembly, and Dynamics of Marine Holobionts. *Annual Review of Marine Science* **16**:11.1-11.24. doi:10.1146/annurev-marine-022123-104345

Hagen WJH, Wan W, Briggs JAG. 2017. Implementation of a cryo-electron tomography tilt-scheme optimized for high resolution subtomogram averaging. *Journal of Structural Biology* **197**:191–198. doi:10.1016/j.jsb.2016.06.007

Hodgskiss LH, Melcher M, Kerou M, Chen W, Ponce-Toledo RI, Savvides SN, Wienkoop S, Hartl M, Schleper C. 2023. Unexpected complexity of the ammonia monooxygenase in archaea. *The ISME Journal* **17**:588-599. doi:10.1038/s41396-023-01367-3

Izumi CMS, Temperini MLA. 2010. FT-Raman investigation of biodegradable polymers: Poly(3-hydroxybutyrate) and poly(3-hydroxybutyrate-co-3-hydroxyvalerate). *Vibrational Spectroscopy*, A Selection of Papers Presented at the 1st Brazilian Meeting on Raman Spectroscopy (BMRS-1) **54**:127–132. doi:10.1016/j.vibspec.2010.07.011

Johnson J, Tolar BB, Tosun B, Yoshikuni Y, Francis CA, Wakatsuki S, DeMirci H. 2023. Crystal Structure of 4-Hydroxybutyryl-CoA Synthetase (ADP-forming): A Key Enzyme in the Thaumarchaeal Hydroxypropionate/Hydroxybutyrate cycle. *bioRxiv*. doi:10.1101/2023.07.14.549078

Kim J-G, Kim S-J, Cvirkaite-Krupovic V, Yu W-J, Gwak J-H, López-Pérez M, Rodriguez-Valera F, Krupovic M, Cho J-C, Rhee S-K. 2019. Spindle-shaped viruses infect marine ammonia-oxidizing thaumarchaea. *Proc Natl Acad Sci USA* **116**:15645–15650. doi:10.1073/pnas.1905682116

Kitzinger K, Marchant HK, Bristow LA, Herbold CW, Padilla CC, Kidane AT, Littmann S, Daims H, Pjevac P, Stewart FJ, Wagner M, Kuypers MMM. 2020. Single cell analyses reveal contrasting life strategies of the two main nitrifiers in the ocean. *Nat Commun* **11**:767. doi:10.1038/s41467-020-14542-3

Kitzinger K, Padilla CC, Marchant HK, Hach PF, Herbold CW, Kidane AT, Konneke M, Littmann S, Mooshammer M, Niggemann J, Petrov S, Richter A, Stewart FJ, Wagner M, Kuypers MMM, Bristow LA. 2019. Cyanate and urea are substrates for nitrification by Thaumarchaeota in the marine environment. *Nat Microbiol* **4**:234–243. doi:10.1038/s41564-018-0316-2

Konneke M, Bernhard AE, de la Torre JR, Walker CB, Waterbury JB, Stahl DA. 2005. Isolation of an autotrophic ammonia-oxidizing marine archaeon. *Nature* **437**:543–6. doi:10.1038/nature03911

Konneke M, Schubert DM, Brown PC, Hugler M, Standfest S, Schwander T, Schada von Borzyskowski L, Erb TJ, Stahl DA, Berg IA. 2014. Ammonia-oxidizing archaea use the most energy-efficient aerobic pathway for CO2 fixation. *Proc Natl Acad Sci U S A* **111**:8239–44. doi:10.1073/pnas.1402028111

Kraft B, Jehmlich N, Larsen M, Bristow LA, Könneke M, Thamdrup B, Canfield DE. 2022. Oxygen and nitrogen production by an ammonia-oxidizing archaeon. *Science* **375**:97–100. doi:10.1126/science.abe6733

Kremer JR, Mastronarde DN, McIntosh JR. 1996. Computer Visualization of Three-Dimensional Image Data Using IMOD. *Journal of Structural Biology* **116**:71–76. doi:10.1006/jsbi.1996.0013

Law KP, He W, Tao J, Zhang C. 2021a. A Novel Approach to Characterize the Lipidome of Marine Archaeon *Nitrosopumilus maritimus* by Ion Mobility Mass Spectrometry. *Frontiers in Microbiology* **12**.

Law KP, He W, Tao J, Zhang C. 2021b. Characterization of the Exometabolome of *Nitrosopumilus maritimus* SCM1 by Liquid Chromatography–Ion Mobility Mass Spectrometry. *Frontiers in Microbiology* **12**.

Leavitt WD, Kopf SH, Weber Y, Chiu B, McFarlin JM, Elling FJ, Hoeft-McCann S, Pearson A. 2023. Controls on the hydrogen isotope composition of tetraether lipids in an autotrophic ammonia-oxidizing marine archaeon. *Geochimica et Cosmochimica Acta* **352**:194-210. doi:10.1016/j.gca.2023.04.033

Lechaire J, Shillito B, Frébourg G, Gaill F. 2002. Elemental characterization of microorganism granules by EFTEM in the tube wall of a deep‐sea vent invertebrate. *Biology of the Cell* **94**:243–249. doi:10.1016/s0248-4900(02)01199-1

Li P-N, Herrmann J, Tolar BB, Poitevin F, Ramdasi R, Bargar JR, Stahl DA, Jensen GJ, Francis CA, Wakatsuki S, van den Bedem H. 2018. Nutrient transport suggests an evolutionary basis for charged archaeal surface layer proteins. *The ISME Journal* **12**:2389–2402. doi:10.1038/s41396-018-0191-0

Lipp JS, Morono Y, Inagaki F, Hinrichs K-U. 2008. Significant contribution of Archaea to extant biomass in marine subsurface sediments. *Nature* **454**:991–994. doi:10.1038/nature07174

Liu Y-T, Zhang H, Wang H, Tao C-L, Bi G-Q, Zhou ZH. 2022. Isotropic reconstruction for electron tomography with deep learning. *Nat Commun* **13**:6482. doi:10.1038/s41467-022-33957-8

Martens-Habbena W, Berube PM, Urakawa H, de la Torre JR, Stahl DA. 2009. Ammonia oxidation kinetics determine niche separation of nitrifying Archaea and Bacteria. *Nature* **461**:976–979. doi:10.1038/nature08465

Martikainen PJ. 2022. Heterotrophic nitrification – An eternal mystery in the nitrogen cycle. *Soil Biology and Biochemistry* **168**:108611. doi:10.1016/j.soilbio.2022.108611

Mastronarde DN. 2003. SerialEM: A Program for Automated Tilt Series Acquisition on Tecnai Microscopes Using Prediction of Specimen Position. *Microsc Microanal* **9**:1182–1183. doi:10.1017/s1431927603445911

McGlynn SE, Chadwick GL, O'Neill A, Mackey M, Thor A, Deerinck TJ, Ellisman MH, Orphan VJ. 2018. Subgroup Characteristics of Marine Methane-Oxidizing ANME-2 Archaea and Their Syntrophic Partners as Revealed by Integrated Multimodal Analytical Microscopy. *Appl Environ Microbiol* **84**:e00399-18. doi:10.1128/AEM.00399-18

Ng K-H, Srinivas V, Srinivasan R, Balasubramanian M. 2013. The *Nitrosopumilus maritimus* CdvB, but Not FtsZ, Assembles into Polymers. *Archaea* **2013**:1–10. doi:10.1155/2013/104147

Parsons AJ, Ahmed I, Rudd CD, Cuello GJ, Pellegrini E, Richard D, Johnson MR. 2010. Neutron scattering and*ab initio*molecular dynamics study of cross-linking in biomedical phosphate glasses. *J Phys: Condens Matter* **22**:485403. doi:10.1088/0953-8984/22/48/485403

Pelve EA, Lindås A-C, Martens-Habbena W, de la Torre JR, Stahl DA, Bernander R. 2011. Cdv-based cell division and cell cycle organization in the thaumarchaeon *Nitrosopumilus maritimus*. *Molecular Microbiology* **82**:555–566. doi:10.1111/j.1365-2958.2011.07834.x

Qin W, Amin SA, Lundeen RA, Heal KR, Martens-Habbena W, Turkarslan S, Urakawa H, Costa KC, Hendrickson EL, Wang T, Beck DA, Tiquia-Arashiro SM, Taub F, Holmes AD, Vajrala N, Berube PM, Lowe TM, Moffett JW, Devol AH, Baliga NS, Arp DJ, Sayavedra-Soto LA, Hackett M, Armbrust EV, Ingalls AE, Stahl DA. 2018. Stress response of a marine ammonia-oxidizing archaeon informs physiological status of environmental populations. *The ISME Journal* **12**:508–519. doi:10.1038/ismej.2017.186

Qin W, Amin SA, Martens-Habbena W, Walker CB, Urakawa H, Devol AH, Ingalls AE, Moffett JW, Armbrust EV, Stahl DA. 2014. Marine ammonia-oxidizing archaeal isolates display obligate mixotrophy and wide ecotypic variation. *Proc Natl Acad Sci U S A* **111**:12504–9. doi:10.1073/pnas.1324115111

Qin W, Heal KR, Ramdasi R, Kobelt JN, Martens-Habbena W, Bertagnolli AD, Amin SA, Walker CB, Urakawa H, Konneke M, Devol AH, Moffett JW, Armbrust EV, Jensen GJ, Ingalls AE, Stahl DA. 2017. *Nitrosopumilus maritimus* gen. nov., sp. nov., *Nitrosopumilus cobalaminigenes* sp. nov., *Nitrosopumilus oxyclinae* sp. nov., and *Nitrosopumilus ureiphilus* sp. nov., four marine ammonia-oxidizing archaea of the phylum Thaumarchaeota. *Int J Syst Evol Microbiol* **67**:5067–5079. doi:10.1099/ijsem.0.002416

Qin W, Zheng Y, Zhao F, Wang Y, Urakawa H, Martens-Habbena W, Liu H, Huang X, Zhang X, Nakagawa T, Mende DR, Bollmann A, Wang B, Zhang Y, Amin SA, Nielsen JL, Mori K, Takahashi R, Virginia Armbrust E, Winkler M-KH, DeLong EF, Li M, Lee P-H, Zhou J, Zhang C, Zhang T, Stahl DA, Ingalls AE. 2020. Alternative strategies of nutrient acquisition and energy conservation map to the biogeography of marine ammonia-oxidizing archaea. *The ISME Journal* **14**:2595–2609. doi:10.1038/s41396-020-0710-7

Remonsellez F, Orell A, Jerez CA. 2006. Copper tolerance of the thermoacidophilic archaeon *Sulfolobus metallicus*: possible role of polyphosphate metabolism. *Microbiology* **152**:59–66. doi:10.1099/mic.0.28241-0

Ring G, Eichler J. 2001. Characterization of Inverted Membrane Vesicles from the Halophilic Archaeon Haloferax volcanii. *Journal of Membrane Biology* **183**:195–204. doi:10.1007/s00232-001-0067-4

Rudnick H, Hendrich S, Pilatus U, Blotevogel K-H. 1990. Phosphate accumulation and the occurrence of polyphosphates and cyclic 2,3-diphosphoglycerate in Methanosarcina frisia. *Arch Microbiol* **154**. doi:10.1007/BF00248840

Sarkar P, Shukla MR, Kumbhar P, Manjre S, Dasgupta S, Bhakthavatsalam V. 2021. Intracellular Localization of Micronutrients in Algae Cells Using Scanning Transmission Electron Microscopy–Energy-Dispersive X-ray Spectroscopy (STEM-EDX) In: Ghosal P, Carter CB, Vinothkumar KR, Sarkar R, editors. Applications of Microscopy in Materials and Life Sciences, Springer Proceedings in Materials. Singapore: Springer. pp. 203–210. doi:10.1007/978-981-16-2982-2_20

Scherer PA, Bochem H-P. 1983. Ultrastructural investigation of 12 Methanosarcinae and related species grown on methanol for occurrence of polyphosphatelike inclusions. *Can J Microbiol* **29**:1190–1199. doi:10.1139/m83-182

Shalev Y, Turgeman-Grott I, Tamir A, Eichler J, Gophna U. 2017. Cell Surface Glycosylation Is Required for Efficient Mating of Haloferax volcanii. *Frontiers in Microbiology* **8**. doi:10.3389/fmicb.2017.01253

Shin DS, Pratt AJ, Tainer JA. 2014. Archaeal Genome Guardians Give Insights into Eukaryotic DNA Replication and Damage Response Proteins. *Archaea* **2014**:1–24. doi:10.1155/2014/206735

580 Spang A, Poehlein A, Offre P, Zumbrägel S, Haider S, Rychlik N, Nowka B,
581 Schmeisser C, Lebedeva EV, Rattei T, Böhm C, Schmid M, Galushko A,
582 Hatzenpichler R, Weinmaier T, Daniel R, Schleper C, Spieck E, Streit W, Wagner
583 M. 2012. The genome of the ammonia-oxidizing Candidatus *Nitrososphaera*
584 *gargensis*: insights into metabolic versatility and environmental adaptations.
585 *Environmental Microbiology* **14**:3122–3145. doi:10.1111/j.1462-
586 2920.2012.02893.x

587 Stahl DA, de la Torre JR. 2012. Physiology and Diversity of Ammonia-Oxidizing
588 Archaea. *Annu Rev Microbiol* **66**:83–101. doi:10.1146/annurev-micro-092611-
589 150128

590 Tamir A, Eichler J. 2017. N-Glycosylation Is Important for Proper Haloferax
591 volcanii S-Layer Stability and Function. *Appl Environ Microbiol* **83**:e03152-16.
592 doi:10.1128/AEM.03152-16

593 Tocheva EI, Dekas AE, McGlynn SE, Morris D, Orphan VJ, Jensen GJ. 2013.
594 Polyphosphate Storage during Sporulation in the Gram-Negative Bacterium
595 Acetonema longum. *Journal of Bacteriology* **195**:3940–3946.
596 doi:10.1128/JB.00712-13

597 Toso DB, Henstra AM, Gunsalus RP, Zhou ZH. 2011. Structural, mass and
598 elemental analyses of storage granules in methanogenic archaeal cells.
599 *Environmental Microbiology* **13**:2587–2599. doi:10.1111/j.1462-
600 2920.2011.02531.x

601 Toso DB, Javed MM, Czornyj E, Gunsalus RP, Zhou ZH. 2016. Discovery and
602 Characterization of Iron Sulfide and Polyphosphate Bodies Coexisting in
603 *Archaeoglobus fulgidus* Cells. *Archaea* **2016**:1–11. doi:10.1155/2016/4706532

604 Urakawa H, Martens-Habbena W, Stahl DA. 2011. Physiology and Genomics of
605 Ammonia-Oxidizing Archaea Nitrification. John Wiley & Sons, Ltd. pp. 115–155.

606 van Wolferen M, Pulschen AA, Baum B, Gribaldo S, Albers S-V. 2022. The cell
607 biology of archaea. *Nat Microbiol* **7**:1744-1755. doi:10.1038/s41564-022-01215-8

608 Walker CB, de la Torre JR, Klotz MG, Urakawa H, Pinel N, Arp DJ, Brochier-
609 Armanet C, Chain PS, Chan PP, Gollabgir A, Hemp J, Hugler M, Karr EA,
610 Konneke M, Shin M, Lawton TJ, Lowe T, Martens-Habbena W, Sayavedra-Soto
611 LA, Lang D, Sievert SM, Rosenzweig AC, Manning G, Stahl DA. 2010.
612 *Nitrosopumilus maritimus* genome reveals unique mechanisms for nitrification
613 and autotrophy in globally distributed marine crenarchaea. *Proc Natl Acad Sci U*
614 *S A* **107**:8818–23. doi:10.1073/pnas.0913533107

615 Wan XS, Hou L, Kao S-J, Zhang Y, Sheng H-X, Shen H, Tong S, Qin W, Ward
616 BB. 2023. Pathways of N_2O production by marine ammonia-oxidizing archaea
617 determined from dual-isotope labeling. *Proc Natl Acad Sci USA*
618 **120**:e2220697120. doi:10.1073/pnas.2220697120

619 Wang Y, Xu J, Cui D, Kong L, Chen S, Xie W, Zhang C. 2021. Classification and
620 Identification of Archaea Using Single-Cell Raman Ejection and Artificial
621 Intelligence: Implications for Investigating Uncultivated Microorganisms. *Anal*
622 *Chem* **93**:17012–17019. doi:10.1021/acs.analchem.1c03495

623 Ward SK, Heintz JA, Albrecht RM, Talaat AM. 2012. Single-Cell Elemental
624 Analysis of Bacteria: Quantitative Analysis of Polyphosphates in Mycobacterium
625 tuberculosis. *Frontiers in Cell and Infection Microbiology* **2**.
626 doi:10.3389/fcimb.2012.00063

627 Xing H, Taniguchi R, Khusainov I, Kreysing JP, Welsch S, Turoňová B, Beck M.
628 2023. Translation dynamics in human cells visualized at high resolution reveal
629 cancer drug action. *Science* **381**:70–75. doi:10.1126/science.adh1411

630 Xue L, Lenz S, Zimmermann-Kogadeeva M, Tegunov D, Cramer P, Bork P,
631 Rappsilber J, Mahamid J. 2022. Visualizing translation dynamics at atomic detail
632 inside a bacterial cell. *Nature* **610**:205–211. doi:10.1038/s41586-022-05255-2

633 Yang Y, Zhang C, Lenton TM, Yan X, Zhu M, Zhou M, Tao J, Phelps TJ, Cao Z.
634 2021. The Evolution Pathway of Ammonia-Oxidizing Archaea Shaped by Major
635 Geological Events. *Molecular Biology and Evolution* **38**:3637–3648.
636 doi:10.1093/molbev/msab129

637 Yin Z, Bi X, Xu C. 2018. Ammonia-Oxidizing Archaea (AOA) Play with Ammonia-
638 Oxidizing Bacteria (AOB) in Nitrogen Removal from Wastewater. *Archaea*
639 **2018**:1–9. doi:10.1155/2018/8429145

640 Zheng SQ, Palovcak E, Armache J-P, Verba KA, Cheng Y, Agard DA. 2017.
641 MotionCor2: anisotropic correction of beam-induced motion for improved cryo-
642 electron microscopy. *Nat Methods* **14**:331–332. doi:10.1038/nmeth.4193

643